A Modulation Method to Realize Sinusoidal Line Current for Bidirectional Isolated Three-Phase AC/DC Dual-Active-Bridge Converter Based on Matrix Converter

Koji Shigeuchi, Jin Xu, *Member, IEEE*, Noboru Shimosato, *Member, IEEE*, and Yukihiko Sato, *Member, IEEE*

***Abstract*—A high-frequency link three-phase ac/dc converter based on matrix converter is widely studied because of its small size of passive components, and some modulation methods have been proposed. However, these methods have not achieved zero-voltage-switching (ZVS) and sinusoidal line currents under bidirectional operation with *PQ* control. This article presents a new modulation method to realize ZVS and sinusoidal line currents under bidirectional operation by accurate control parameters (duty cycle and phase shift) for high-frequency link bidirectional three-phase ac/dc dual-active-bridge (DAB) converter. The converter can realize ZVS by phase-shift-modulation similarly to the dc/dc DAB converter. The line currents have nonlinear characteristics to phase shift and duty cycle. Therefore, the proposed method uses a nonlinear mathematical model to determine the accurate duty cycle and phase shift in order to realize sinusoidal line currents. The accurate duty cycle and phase shift are determined by real-time numerical calculation. Experimental results employing a 1-kW laboratory prototype verify the capability to control active and reactive power with sinusoidal line current. It is confirmed that the proposed method can realize the sinusoidal line current with total harmonic distortion of less than 4% under the bidirectional operating condition at the rated power.**

***Index Terms*—AC–AC converters, ac–dc power converters, battery chargers, dc–ac power converters, matrix converters.**

I. INTRODUCTION

RECENTLY, a lot of renewable energy systems, such as wind power generation and photovoltaic system, have been introduced for solving environmental issues. Because those systems have large fluctuation of the power generation, it may affect stability of the power grid. The battery energy storage systems are studied as a method to solve this problem [1]. For connection of the battery energy storage systems to the power grid, a bidirectional isolated ac/dc converter, which realizes high efficiency, small size, low cost and good power quality, is needed [2]. A high-frequency link ac/dc converter has been widely studied because of the small size of transformer. A typical-type high-frequency link ac/dc converter is configured by a non-isolated ac/dc converter and a high-frequency isolated dc/dc converter [3]–[5]. However, such converters require a dc link electrolytic capacitor that has problems of large size and short lifetime. To overcome these problems, several types of ac/dc converters applying matrix converter (MC) have been proposed [6]–[23]. Since those converters do not have a dc link, the electrolytic capacitors are not necessary. Therefore, a small-size and long-lifetime system can be realized.

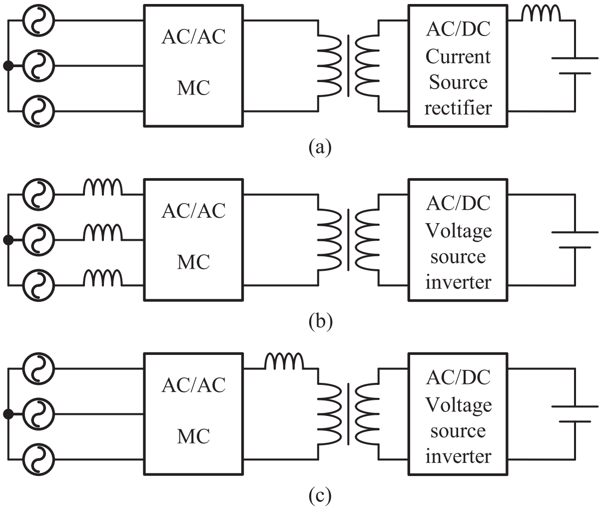

Fig. 1. Basic topologies of high-frequency link isolated three-phase ac/dc converter based on matrix converter. (a) Buck type. (b) Boost type. (c) Dual-active-bridge type.

Buck type [6]–[8], boost type [9]–[11] and dual-active-bridge (DAB) type [12]–[23] ac/dc converters based on matrix converter have been proposed. Fig. 1 shows the basic topologies of each type. The buck type and boost type topologies are based on current source pulsewidth modulation (PWM) rectifier and

---

Manuscript received February 3, 2020; revised July 21, 2020; accepted September 9, 2020. Date of publication September 25, 2020; date of current version January 22, 2021. This paper was presented in part at the 2018 International Power Electronics Conference, Toki Messe, Niigata, Japan, May 23, 2018. Recommended for publication by Associate Editor J. Clare. *(Corresponding author: Koji Shigeuchi.)*

Koji Shigeuchi and Yukihiko Sato are with the Faculty of Engineering, Chiba University, Chiba 263-8522, Japan (e-mail: kshigeuchi125@gmail.com; ysato@faculty.chiba-u.jp).

Jin Xu and Noboru Shimosato are with the Myway Plus Corporation, Yokohama 220-0022, Japan (e-mail: jin_xu@myway.co.jp; shimosato@myway.co.jp).

Color versions of one or more of the figures in this article are available online at https://ieeexplore.ieee.org.

Digital Object Identifier 10.1109/TPEL.2020.3026977

voltage source PWM inverter (INV), respectively. The buck type can realize zero voltage switching (ZVS) in ac to dc conversion and the boost type can realize ZVS in dc to ac conversion by using a leakage inductance of the high-frequency transformer [10], [11]. However, in the case of reverse direction conversion, ZVS in all the power switches cannot be realized. In addition, voltage spike occurs by the leakage inductance. Therefore, those two types are considered unsuitable for bidirectional operation.

In the DAB-type topology, both of the MC and voltage source INV on the secondary side generate high frequency link voltage at the same time. This operation is based on a principle of dc/dc DAB converter [24], [25]. The dc/dc DAB converter is actively investigated because the converter can realize ZVS in all power switches under bidirectional operation. For the same reason, it is expected that the DAB-type ac/dc converter is suitable for bidirectional operation [12].

Several modulation methods for three-phase ac/dc DAB converter have been proposed. However, those methods still have some problems. In [13], a modulation method to realize bidirectional active power flow control with sinusoidal line current under zero current switching (ZCS) has been proposed. However, the power factor of the high-frequency link is very low, and conduction losses are nearly twice as large as typical high-frequency link ac/dc converter (voltage source INV and DAB system) [14]. In [15] and [16], a modulation method has been proposed, and active power control under ZVS is achieved. This modulation method uses square-wave approximation to obtain duty cycle with reduced calculation burden. However, this approximation method increases the line current distortion and it has reported that the total harmonic distortion (THD) of line current is higher than 10% under all conditions. In [17], an improved technique of the method [15] has been proposed. The compensated trapezoidal approximation has been introduced to determine the control parameters that realize sinusoidal line currents. In addition, power factor correction (PFC) technique has been proposed, and unity power factor has been achieved. However, the line current THD is not low enough due to the limited effect of the compensation. In [18], in order to calculate accurate control parameters, a modulation method that uses the ripple cancellation of the active current during one switching period has been proposed. However, a higher number of switching is required to realize the ripple cancellation. In addition, this method cannot realize ZVS. Thus, the switching losses may increase significantly. In [19]–[21], the methods using space vector modulation have been proposed. They use two adjacent switching periods as one control period to calculate the accurate control parameter easily because the first and second half period control the line current of each input phases independently. In [21], the active power and reactive power flow control are realized, and [22] has proposed a control method to improve the control performance. However, in these space vector-based modulation methods, ZVS in all power switches is not achieved because of the constraint of current at the instants of switching. Moreover, the current of the high-frequency transformer becomes larger than the ordinal method ([15]–[18]), resulting in larger conduction loss. In [23], ZVS/ZCS modulation method achieving sinusoidal line currents has been proposed. This method uses four of the control parameters that are obtained by offline numerical optimization and three-dimensional lookup-table (LUT) and trilinear interpolation. It is reported that the sampling point is 30 per dimension, resulting a total of 27 000 entries corresponding to the four control parameter. High-efficiency and low line current THD are reported. However, bidirectional operation has not been validated with this method. Moreover, reactive power control has not been realized. To include reactive power control, the LUT must have four dimensions, and the total operating points for the control parameter storage may increase dramatically to $30 \times 30 \times 30 \times 30$ and the interpolation may require a heavy calculation.

This article proposes a new modulation method based on PWM and phase-shift-modulation (PSM) for bidirectional isolated three-phase ac/dc DAB converter. This method realizes bidirectional active and reactive power flow control with sinusoidal line current waveform. The line currents have nonlinear characteristics to the control variables (duty cycle and phase shift). To overcome this problem, the proposed method obtains the accurate duty cycle and phase shift that achieve sinusoidal line current waveform by using nonlinear system mathematical models and real-time numerical calculation. In addition, ZVS in all the power switches can be realized.

The fundamentals of the proposed modulation have been reported in a previous conference paper [26]. This article is reconfigured comprehensively by adding the several important contents, such as the harmonic analysis of the line current, the validation of the dynamic performance with *PQ* control, the comparison with the existing methods, and the detailed analisis of the system loss.

The rest of this article is organized as follows. Section II presents the outline of the modulation strategy to realize active and reactive power control with sinusoidal line current waveforms. Section III introduces the details of the system mathematical models and explains the numerical calculation method to obtain the accurate duty cycle and phase shift. Section IV presents the simulation results for validating dynamic performance, efficiency, and line current THD. Finally, to demonstrate the validity of the proposed modulation method, experimental results employing a laboratory 1-kW prototype are presented and discussed in Section V.

II. MODULATION METHOD

A. *Circuit Configuration*

Fig. 2 shows a circuit configuration of a bidirectional ac/dc DAB converter. The primary side is composed of a three-phase to single-phase MC, an input *LC* filter, and a clamp circuit. The secondary side consists of a full-bridge INV. A high-frequency transformer is connected with an external inductor L in series. The MC input currents i_u, i_v, and i_w have a lot of harmonics of the switching frequency. Therefore, input *LC* filter is inserted between the ac input and MC to attenuate these harmonics. The basic operation of MC is summarized as follows. The MC connects any two of the input phases of U, V, and W to the output terminals P and N. For example, when U and W are connected to P and N, respectively, then the MC output voltage v_MC equals to $e_\mathrm{u}-e_\mathrm{w}$. Here, e_u, e_v, e_w are the input phase voltages having by

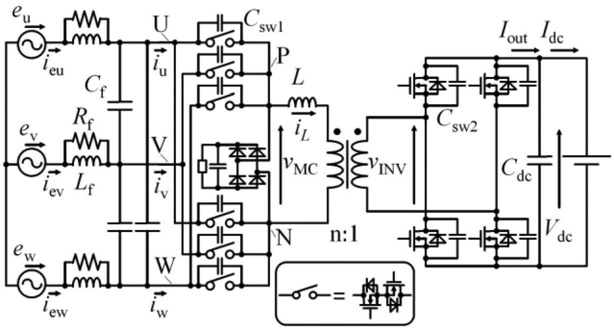

Fig. 2. Bidirectional isolated three-phase ac/dc DAB converter based on matrix converter.

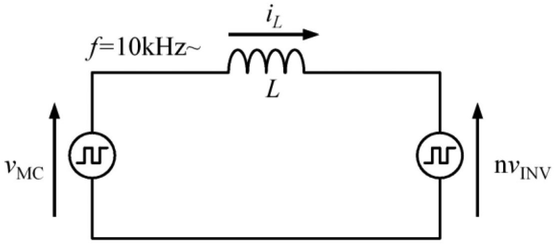

Fig. 3. Equivalent circuit of high-frequency link.

commercial line angular frequency ω and line voltage *E* given by the following equations:

$$\begin{bmatrix} e_u \\ e_v \\ e_w \end{bmatrix} = \sqrt{\frac{2}{3}} E \begin{bmatrix} \cos(\omega t) \\ \cos(\omega t - 2\pi/3) \\ \cos(\omega t - 4\pi/3) \end{bmatrix}. \tag{1}$$

At the same time, the transformer current i_L flows through *U* and *W* phases, and input currents i_u and i_w satisfy $i_u = i_L$ and $i_w = -i_L$, respectively. In this case, since *V* phase is not connected to any terminal, *V* phase input current i_v equals to 0.

B. Proposed Modulation Strategy

This section presents the proposed modulation strategy to realize active and reactive power control with sinusoidal line current waveforms. Fig. 3 shows the equivalent circuit of the high-frequency link part. The difference between the MC output voltage v_{MC} and the INV output voltage nv_{INV} is applied to the inductor *L*. Here, nv_{INV} is referred to the primary side, and n is turns ratio of the high-frequency transformer. In addition, the magnetization current of the transformer is assumed to be negligible.

In the following explanation, the input phase voltages e_u, e_v, e_w are assumed to have a relationship as $e_u > e_v > e_w$. If both the MC and INV generate square wave voltages with a phase shift, the average input power *P* is obtained as follows:

$$P = \frac{e_M n V_{dc}}{2fL} \frac{\delta}{\pi} \left(1 - \frac{\delta}{\pi}\right). \tag{2}$$

Here, δ is phase shift between v_{MC} and v_{INV}, and the voltage e_M is the amplitude of the MC output voltage v_{MC} that equals to $e_M = e_u - e_w$, and V_{dc} is the amplitude of the INV output voltage v_{INV}. Equation (2) shows that the active power *P* is controllable by adjusting phase shift δ. However, if the MC generates the square wave voltage e_M, *V* phase is not connected to the output terminals of the MC. In this case, the sinusoidal line current waveform cannot be achieved because the current does not flow through *V* phase. To overcome this problem, PWM is applied to the MC. Fig. 4 shows the outline of the modulation waveforms based on PWM and PSM. In Fig. 4, the waveforms of the MC and INV output voltages v_{MC} and v_{INV}, the high-frequency transformer current i_L, and the MC input currents i_u, i_v, i_w are shown. The MC generates e_M and e_m ($= e_v - e_w$ or $e_u - e_v$). Here, d_m is defined as the duty cycle when the MC outputs $\pm e_m$ in one switching period. When the MC generates e_m, the transformer current i_L flows through *V* phase, and the *V* phase input current i_v equals to i_L or $-i_L$. Therefore, the average MC input current of *V* phase $\overline{i_v}$ is controllable by adjusting the duty cycle d_m. In addition, when the input power *P* and *V* phase input current i_v are controlled, the MC input currents of *U* phase and *W* phase are indirectly determined because the relationship of the following equations exists:

$$\begin{cases} P = \overline{i_u} e_u + \overline{i_v} e_v + \overline{i_w} e_w \\ 0 = \overline{i_u} + \overline{i_v} + \overline{i_w} \end{cases} \tag{3}$$

In this way, the waveforms of line currents i_{eu}, i_{ev}, i_{ew} can become sinusoidal by controlling *P* and $\overline{i_v}$ to appropriate values because i_{eu}, i_{ev}, i_{ew} are almost equal to the MC average input currents $\overline{i_u}, \overline{i_v}, \overline{i_w}$. The reference values of the line currents i^*_{eu}, i^*_{ev}, and i^*_{ew} are determined by given values of an input power reference *P** and a power factor angle reference α^* as follows:

$$\begin{bmatrix} i^*_{eu} \\ i^*_{ev} \\ i^*_{ew} \end{bmatrix} = \sqrt{\frac{2}{3}} \frac{P^*}{E\cos(\alpha^*)} \begin{bmatrix} \cos(\omega t - \alpha^*) \\ \cos(\omega t - 2\pi/3 - \alpha^*) \\ \cos(\omega t - 4\pi/3 - \alpha^*) \end{bmatrix}. \tag{4}$$

Since α^* has relationship to reactive power reference *Q** as following equation, it can be also possible to determine $i^*_{eu}, i^*_{ev}, i^*_{ew}$ by given *P** and *Q**:

$$Q^* = -P^* \tan\alpha^*. \tag{5}$$

In conclusion, the outline of the proposed modulation method is described as follows.

1) Obtain *V* phase input current reference i^*_{ev} from input power reference P^* and power factor angle reference α^*(or input reactive power reference Q^*).
2) Calculate the duty cycle d_m and phase shift δ from the system mathematical model. In other words, solve $P(\delta, d_m) = P^*$ and $\overline{i_v}(\delta, d_m) = i^*_{ev}$.
3) The MC generates PWM waveform modulated with the duty cycle d_m, and the INV generates square waveform modulated with the phase shift δ.

Although the modulation strategy is described under $e_u > e_v > e_w$ conditions in this section, the modulation strategy can be extended to other cases by considering symmetry of three phases. Fig. 5 shows the detail of the amplitudes of the MC output voltages e_M and e_m for each phase.

C. Mathematical Model

To determine the accurate duty cycle d_m and phase shift δ from $P(\delta, d_m) = P^*$ and $\overline{i_v}(\delta, d_m) = i^*_{ev}$, it is necessary to obtain mathematical models of the input power $P(\delta, d_m)$ and *V* phase

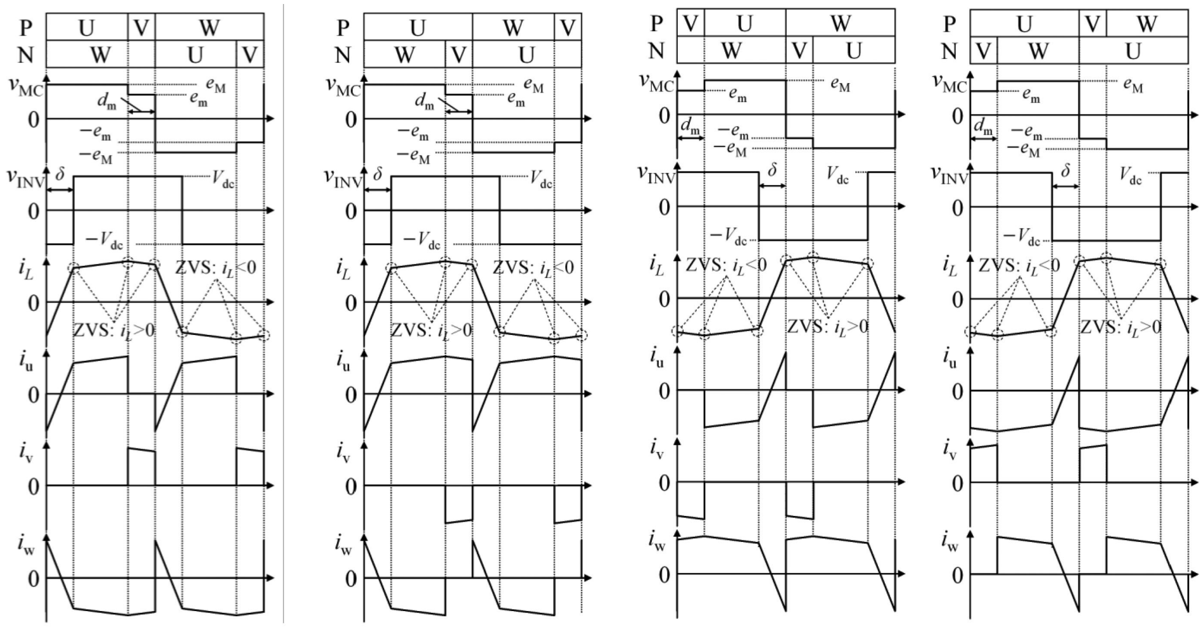

(a) (b) (c) (d)

Fig. 4. Proposed modulation waveforms ($e_{\mathrm{u}} > e_{\mathrm{v}} > e_{\mathrm{w}}$). There are four modes depending on the direction of the power and the sign of the V phase current. Modulation waveforms under each modes: (a) $P^* > 0, i^*_{\mathrm{ev}} > 0$; (b) $P^* > 0, i^*_{\mathrm{ev}} < 0$; (c) $P^* < 0, i^*_{\mathrm{ev}} < 0$; (d) $P^* < 0, i^*_{\mathrm{ev}} > 0$.

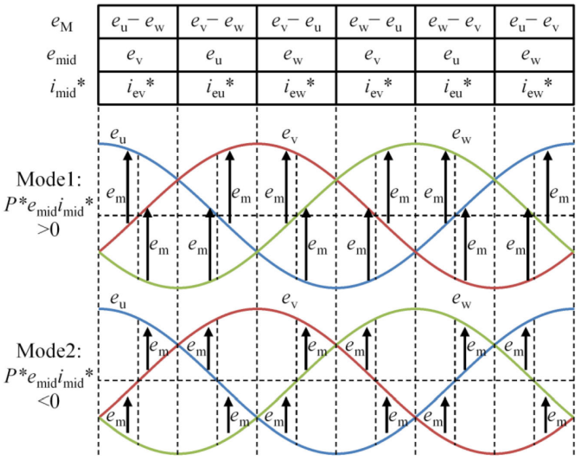

Fig. 5. Detail of the amplitudes of the MC output voltages e_{M} and e_{m} at each phase. e_{M} equals the maximum value of input three phase line-to-line voltages. e_{m} contains the component of the middle voltage of three phase voltages, and has two modes depending on the sign of $P^*e_{\mathrm{mid}}i_{\mathrm{mid}}^*$. In mode1, the directions of the input power derived from the middle voltage phase ($e_{\mathrm{mid}}i_{\mathrm{mid}}^*$) is equal to the input power (P^*), and the power is transferred in the opposite direction in mode 2. When the phase shift angle reference $\alpha^* = 0$, only mode 1 occurs.

average input current $\overline{i_{\mathrm{v}}}(\delta, d_{\mathrm{m}})$. First, the model of the input power $P(\delta, d_{\mathrm{m}})$ is obtained from the system equivalent circuit, as shown in Fig. 3, as follows:

$$P = \frac{e_{\mathrm{M}}\mathrm{n}V_{\mathrm{dc}}}{2fL}\frac{\delta}{\pi}\left(1-\frac{\delta}{\pi}\right) + \frac{(e_{\mathrm{M}}-e_{\mathrm{m}})\,\mathrm{n}V_{\mathrm{dc}}}{4fL}d_{\mathrm{m}}\left(1-2\frac{\delta}{\pi}-d_{\mathrm{m}}\right). \tag{6}$$

In the case that the MC generates square wave, the input power $P(\delta, d_{\mathrm{m}})$ is given by (2). Equation (6) has an extra second term compared to (2). This term corresponds to the effect of PWM. Then, the model of the *V* phase average input current $\overline{i_{\mathrm{v}}}(\delta, d_{\mathrm{m}})$ is obtained from the *V* phase input current i_{v} with the duty cycle d_{m} (see Fig. 4), as follows:

$$|\overline{i_{\mathrm{v}}}| = f\left\{\int_{\frac{1-d_{\mathrm{m}}}{2f}}^{\frac{1}{2f}} i_L(t)\,dt - \int_{\frac{2-d_{\mathrm{m}}}{2f}}^{\frac{1}{f}} i_L(t)\,dt\right\}. \tag{7}$$

The following equation is derived by substituting the transformer current i_L to (7). Here, i_L is calculated based on the equivalent circuit (see Fig. 3) and the waveforms of v_{MC} and v_{INV}, as illustrated in Fig. 4

$$|\overline{i_{\mathrm{v}}}| = \frac{\mathrm{n}V_{\mathrm{dc}}}{2fL}\frac{\delta}{\pi}d_{\mathrm{m}} + \frac{e_{\mathrm{M}}-\mathrm{n}V_{\mathrm{dc}}}{4fL}d_{\mathrm{m}}(1-d_{\mathrm{m}}). \tag{8}$$

Equations (6) and (8) describe the system mathematical models and they have nonlinear characteristics. Finally, the duty cycle d_{m} and phase shift δ are determined by solving equations $P^* = P$ and $i^*_{\mathrm{ev}} = \overline{i_{\mathrm{v}}}$ obtained by (6) and (8). The equations are expressed as follows:

$$P^* = \frac{e_{\mathrm{M}}\mathrm{n}V_{\mathrm{dc}}}{2fL}\frac{\delta}{\pi}\left(1-\frac{\delta}{\pi}\right) + \frac{(e_{\mathrm{M}}-e_{\mathrm{m}})\,\mathrm{n}V_{\mathrm{dc}}}{4fL}d_{\mathrm{m}}\left(1-2\frac{\delta}{\pi}-d_{\mathrm{m}}\right) \tag{9}$$

$$|i^*_{\mathrm{ev}}| = \frac{nV_{\mathrm{dc}}}{2fL}\frac{\delta}{\pi}d_{\mathrm{m}} + \frac{e_{\mathrm{M}}-\mathrm{n}V_{\mathrm{dc}}}{4fL}d_{\mathrm{m}}(1-d_{\mathrm{m}}). \tag{10}$$

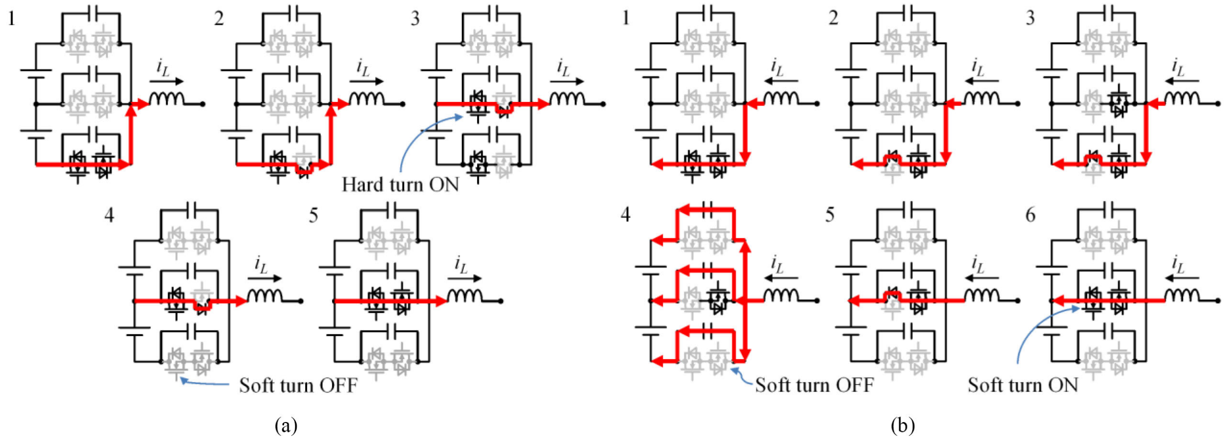

Fig. 6. Commutation to high voltage from low voltage phase of the line under ZVS and hard switching conditions. (a) Hard switching condition. (b) ZVS condition.

D. Zero Voltage Switching

The ac/dc DAB converter can realize ZVS in all the power switches as same as dc/dc DAB converters [15], [25]. ZVS is achieved by turning on a switch when the voltage across the power switch is clamped to zero by conduction of its antiparallel diode. When turning OFF the switch, since the snubber capacitor connected to the power switches suppresses the rising of the voltage, the switching loss is reduced. The ZVS conditions are determined by the direction of i_L. Fig. 6 shows commutations from low voltage phase to high voltage phase under ZVS and hard switching conditions. The waveforms with proposed modulation shown in Fig. 4 meet the ZVS condition in all switching cases. Therefore, the proposed method can realize ZVS in all the power switches.

In the case that the snubber capacitors are not connected, turn-ON losses do not occur but turn-OFF losses occur. However, the total of the switching losses can be reduced because the turn-OFF losses are smaller than the turn-on losses in general. The operating range in which ZVS can be realized is limited actually by power and the voltage ratio between the input and output. In addition, the magnetizing current of the high-frequency transformer expands the ZVS range. These characteristics are the same as the ordinal dc/dc DAB converter.

III. CALCULATION OF DUTY CYCLE AND PHASE SHIFT

A. Numerical Calculation

This subsection presents the solving method for the (9) and (10). It is difficult to solve these equations analytically, because these are nonlinear simultaneous equations. Therefore, to solve the equations, the real-time numerical calculation is introduced. The bisection numerical calculation method is applied due to its high reliability. Bisection method can certainly solve one-variable equation when the two initial values are set suitably based on the outline of the equation. The solving method is summarized as follows.

1) Drop out duty cycle $d_{\rm m}$ from the equations and obtain one-variable equation $P^* = P(\delta)$.
2) Solve equation $P^* = P(\delta)$ by the bisection method.
3) Determine duty cycle $d_{\rm m}$ from the phase shift δ.

To apply the bisection method, the nonlinear simultaneous equations should be converted into a one-variable equation because bisection method cannot be applied to multivariable equations. The duty cycle $d_{\rm m}$ is dropped out from (9) and (10) by solving the following equation which is obtained by dividing (10) by (9)

$$\frac{|i^*_{\rm ev}|}{P^*} = \frac{2\frac{\delta}{\pi}d_{\rm m} + \left(e_{\rm M}/{\rm n}V_{\rm dc} - 1\right)d_{\rm m}\left(1-d_{\rm m}\right)}{2e_{\rm M}\frac{\delta}{\pi}\left(1-\frac{\delta}{\pi}\right) + \left(e_{\rm M}-e_{\rm m}\right)d_{\rm m}\left(1-2\frac{\delta}{\pi}-d_{\rm m}\right)}. \tag{11}$$

By solving equation (11), the duty cycle $d_{\rm m}$ is expressed as following equations:

$$\begin{cases} A = 1 - \frac{e_{\rm M}}{{\rm n}V_{\rm dc}} + e_{\rm M}\frac{|i^*_{\rm ev}|}{P^*}\left(1-\frac{e_{\rm m}}{e_{\rm M}}\right) \\ B = -A + 2\frac{\delta}{\pi}\left\{1 + e_{\rm M}\frac{|i^*_{\rm ev}|}{P^*}\left(1-\frac{e_{\rm m}}{e_{\rm M}}\right)\right\} \\ C = -2e_{\rm M}\frac{|i^*_{\rm ev}|}{P^*}\frac{\delta}{\pi}\left(1-\frac{\delta}{\pi}\right) \\ d_{\rm m}(\delta) = \frac{-B+\sqrt{B^2-4AC}}{2A}. \end{cases} \tag{12}$$

The following equation is obtained by substituting (12) into (9):

$$P^* = \frac{e_{\rm M}{\rm n}V_{\rm dc}}{2fL}\frac{\delta}{\pi}\left(1-\frac{\delta}{\pi}\right) + \frac{\left(e_{\rm M}-e_{\rm m}\right){\rm n}V_{\rm dc}}{4fL}d_{\rm m}(\delta)\left(1-2\frac{\delta}{\pi}-d_{\rm m}(\delta)\right). \tag{13}$$

The right side of this equation is a function of δ, and can be expressed as $P(\delta)$ as follows:

$$P^* = P(\delta). \tag{14}$$

In (14), $P(\delta)$ contains several parameters. Fig. 7 shows the form of $P(\delta)$ for possible variation in all the parameters. In Fig. 7, 1 p.u. corresponds to the maximum power $P_{\rm max} = e_{\rm M}{\rm n}V_{\rm dc}/8fL$. Function form of $P(\delta)$ is similar to a parabola in any cases, and it takes the minimum value 0 p.u. at $\delta = 0$, and it takes the maximum value at 1 p.u. around $\delta = \pi/2$. Therefore, the equation $P^* = P(\delta)$ can be solved by using the bisection method

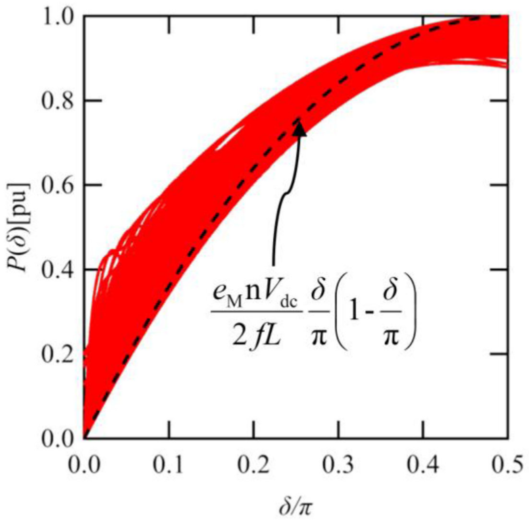

Fig. 7. Function form of $P(\delta)$.

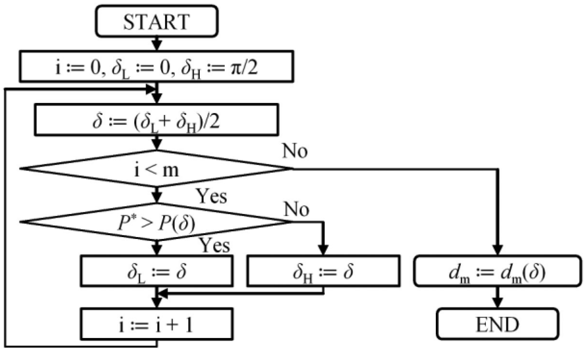

Fig. 8. Flowchart of numerical calculation to determine phase shift δ and duty cycle d_{m} (m is a number of iteration).

setting two initial values δ_{L} and δ_{H} to 0 and $\pi/2$, respectively. The flowchart of the solving method is shown in Fig. 8. The iteration number m is set to reduce enough the error of δ.

Fig. 9 shows the relationship between the line current THD and the iteration number *m* in the calculation with the equivalent circuit model (see Fig. 3). The accuracy of δ is improved as m increases, and the line current THD is reduced. From this results, we can see that the iteration number m = 10 is enough to reduce the line current THD.

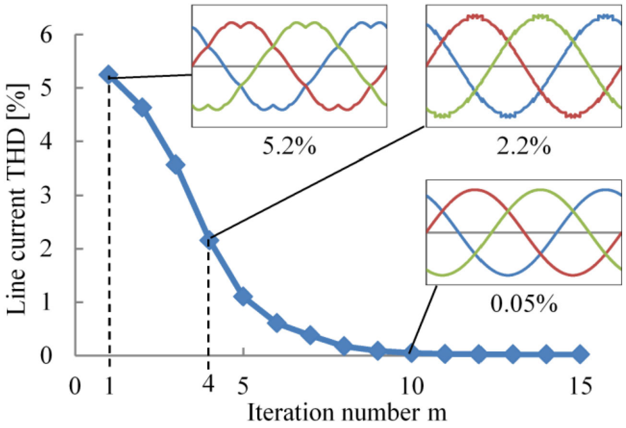

Fig. 9. Relationshio between the line current THD and the iteration number m. Note: this is simulated by the equivalent circuit model (see Fig. 3) that does not include dynamics of the LC filter, switching time and various losses. The simulation condition: $E = 200$ V, $V_{\mathrm{dc}} = 240$ V, n = 1, $f = 100$ kHz, $P^* = 4$kW, $\alpha^* = 0$, and $L = 15$ µH.

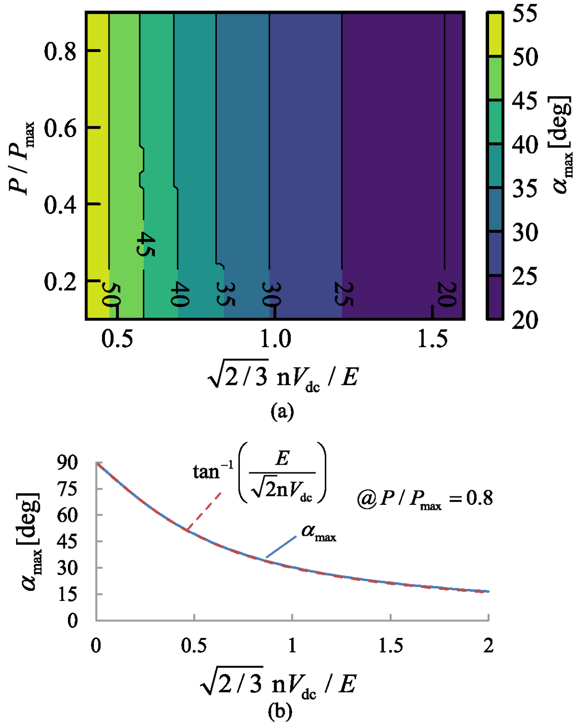

Fig. 10. Characteristics of the maximum controllable power factor angle α_{max}. (a) Overall trend for variation of power and voltage ratio between the input E and output V_{dc}. (b) Result when $P/P_{\mathrm{max}} = 0.8$ extracted from the result in (a).

B. Operation Range

This section presents the possible operation range of the converter when the proposed method is applied. The operation range is limited by the following conditions:

$$\begin{cases} |P^*| \leq P_{\mathrm{max}} \approx \frac{e_{\mathrm{M}} \mathrm{n} V_{\mathrm{dc}}}{8fL} \\ 0 \leq d_{\mathrm{m}} \leq 1 - \frac{\delta}{\pi}. \end{cases} \tag{15}$$

The first and second equations correspond to the operation range of the active power and reactive power, respectively. In other words, the power reference value P^* and the input power factor angle reference value α^* are limited. The maximum controllable α, defined as α_{max}, can be obtained by (1), (4), (12), (14), and (15). But, the derivation of the analytical result is very difficult due to the nonlinear characteristics of these equations. Therefore, α_{max} is calculated numerically and shown in Fig. 10. Fig. 10(a) is the overall trend of the α_{max} for normalized V_{dc} and power P. V_{dc} is normalized with respect to the minimum value of e_{M} ($=\sqrt{3/2}E$) for entire one input voltage period, and P is normalized with respect to P_{max} ($=\sqrt{3/2}E\mathrm{n}V_{\mathrm{dc}}/8fL$). From

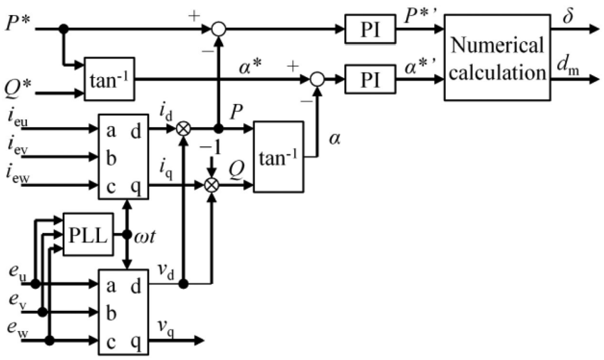

Fig. 11. Block diagram of the closed-loop *PQ* control.

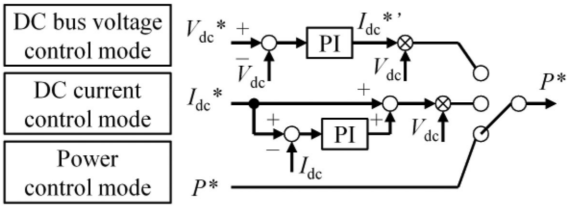

Fig. 12. Block diagram to determine power reference for each control mode.

the result shown in Fig. 10(a), $\alpha_{\max}$ is not affected significantly by *P*. In contrast to this, $\alpha_{\max}$ decreases as $V_{\rm dc}$ increases because the absolute value of i_L in the period of $d_{\rm m}$ is decreased. Under this condition, $d_{\rm m}$ needs to be large and unable to satisfy the second condition in (15). The relationship between $\alpha_{\max}$ and $V_{\rm dc}$ extracted from Fig. 10(a) when $P/P_{\max} = 0.8$ is shown in Fig. 10(b). $\alpha_{\max}$ exceeds 30° at $\sqrt{2/3}{\rm n}V_{\rm dc}/E = 1$. In addition, it can be seen that $\alpha_{\max}$ is almost equal to $\tan^{-1}(E/\sqrt{2}{\rm n}V_{\rm dc})$ under all power conditions.

IV. SIMULATION

A. *Closed-Loop* PQ *Control*

The proposed method can be applied to open loop PFC control by setting α^* based on the input *LC* filter model, that can eliminate the input current sensors. This approach has been proposed in [27] for buck type converter. In this section, more general closed-loop *PQ* control that can control reactive power directly. Fig. 11 shows the block diagram of the proposed closed-loop *PQ* control. The input power *P* and reactive power *Q* are calculated by the input currents $i_{\rm eu}$, $i_{\rm ev}$, $i_{\rm ew}$, and the input phase voltages $e_{\rm u}$, $e_{\rm v}$, $e_{\rm w}$, and the power factor angle α is calculated by *P* and *Q*. They are compared with their reference values, and PI controller calculates P^* and α^* that are used in the numerical calculation to determine the control parameters (δ and $d_{\rm m}$). Fig. 12 shows the block diagram to determine the power reference value in three possible control modes, that is, dc-bus voltage control, dc current control, and power control. To verify applicability of the proposed *PQ* control, a simulation model is implemented by using PSIM. The conditions of the simulation are given in Table I . Fig. 13 shows a simulation result in the case of a step change in *P*. The input power reference P^* is set to 2kW, and is changed to 4 kW at 20 ms, and then changed to −4 kW at 40 ms. The input power *P* tracks well to P^*, and it can be confirmed that changing from ac to dc conversion mode to dc to ac conversion mode is achieved seamlessly. In addition, *Q* is stabilized even under change in P^*. Fig. 14 shows the simulation result of a step change in *Q*. The reactive power reference Q^* is set to 0var, and change to 2 kvar at 20 ms, and then changed to −2 kvar at 40 ms. As well as the case of change in P^*, *Q* tracks well to Q^*, and *P* is stabilized regardless of the change in *Q*. From these results, it can be confirmed that the proposed *PQ* controller can control *P* and *Q* independently. By setting Q^* to 0, the reactive power of

TABLE I
CONDITIONS OF SIMULATION MODEL

Source line voltage	200V, 50Hz
Secondary DC voltage V_{dc}	240V
External inductor *L*	15μH
Input filter L_f, C_f, R_f	150μH, 5.95μF, 10.0Ω
Switching frequency *f*	100kHz
Turns ratio n	1
Rated input power	4kW
Dead time of INV	100ns
Commutation time of MC	100ns

TABLE II
SPECIFICATIONS OF EXPERIMENTAL SYSTEM

Source line voltage	200V, 50Hz
Secondary DC voltage V_{dc}	60V
External inductor *L*	400μH
Input filter L_f, C_f, R_f	0.75mH, 10μF, 16.5Ω
Switching frequency *f*	15.15kHz
Turns ratio n	4
Primary side exciting inductance L_m	> 5.28mH
Primary side Leakage inductance l_{leak}	< 30μH
Rated input power	1kW
Dead time of INV	3μs
Commutation time of MC	1.5μs

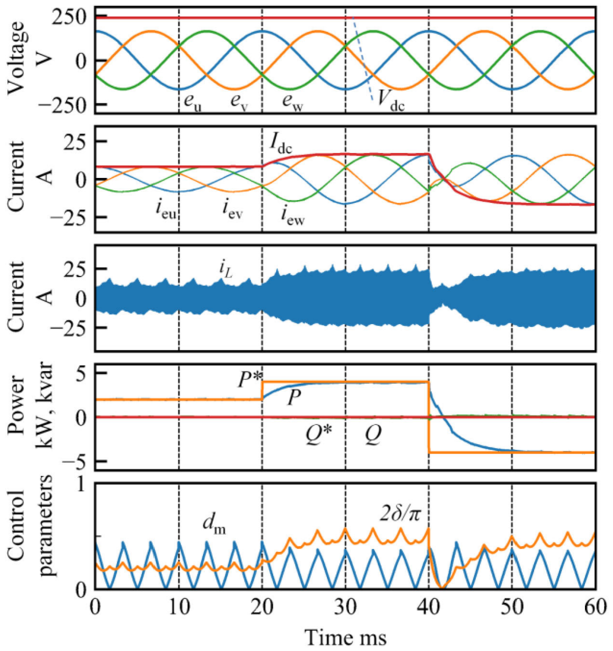

Fig. 13. Simulation result of response to step change in *P*.

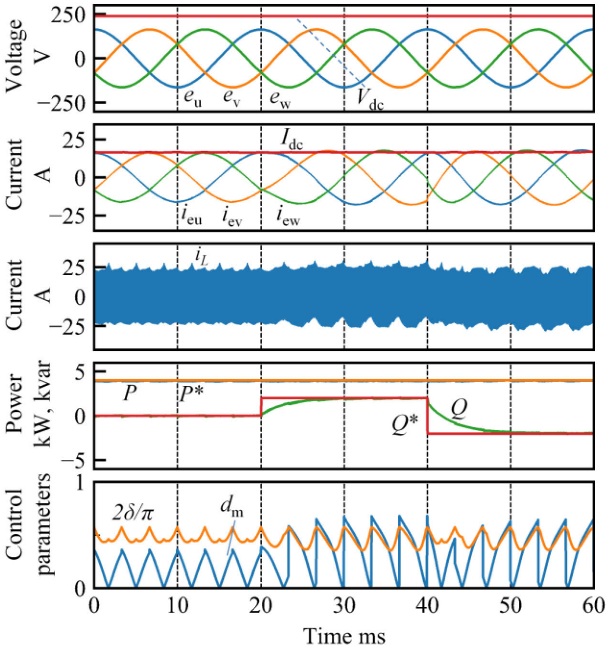

Fig. 14. Simulation result of response to step change in Q.

the LC input filter can be compensated, and unity power factor is realized.

B. Comparison With Existing Modulation Methods

For comparison with existing modulation methods, the simulation based on the equivalent circuit has been performed using Python. The methods chosen for comparison are selected from the existing methods that can control both active and reactive power simultaneously. The simulation waveforms are shown in Fig. 15. The waveforms with the proposed method shown in Fig. 15(a) and those with method in [17] shown in Fig. 15(b) are similar except the waveforms of v_{MC}. In Fig. 15 (b), v_{MC} has zero-voltage periods. This is effective to reduce the conduction losses. However, determination of the control parameter becomes difficult because the degrees of freedom are increased. The method in [17] solves this problem by introducing trapezoidal approximation. On the other hand, the accuracy of the control parameters is low, and distortion of the line current is increased. The method in [21] shown in Fig. 15(c) is different from those in Fig. 15(a) and (b), and two switching periods of the MC and INV are treated as one control period. The first and second pulses control the line current of each phase sequentially, and the accurate control parameter can be determined easily. However, this method does not realize ZVS in all the power switches. In both the MC and INV, switching to zero-voltage occurs at the same time around the end of each control period. At this timing, a hard-switching occurs in the INV (i_L<0) or MC (i_L>0) depending on the direction of the current in the high-frequency link. In addition, the peak of i_L is larger than those in Fig. 15(a) and (b) because when a line current of a phase that is controlled by the second pulse is very small compared with the line current in other phases, most of the power is transferred only by the first pulse. The peak of i_L is 52.9 A which is larger than two times the peak currents with the other two methods. In this way, the rms value of i_L increases, resulting in larger conduction loss compared with the other two methods. Fig. 16 shows the estimated losses and the efficiency with each method. The efficiency with the proposed method is lower than the method in [17] by 0.06%. This difference in the loss may be caused by the zero-voltage period in v_{MC} (see Fig. 15). The efficiency

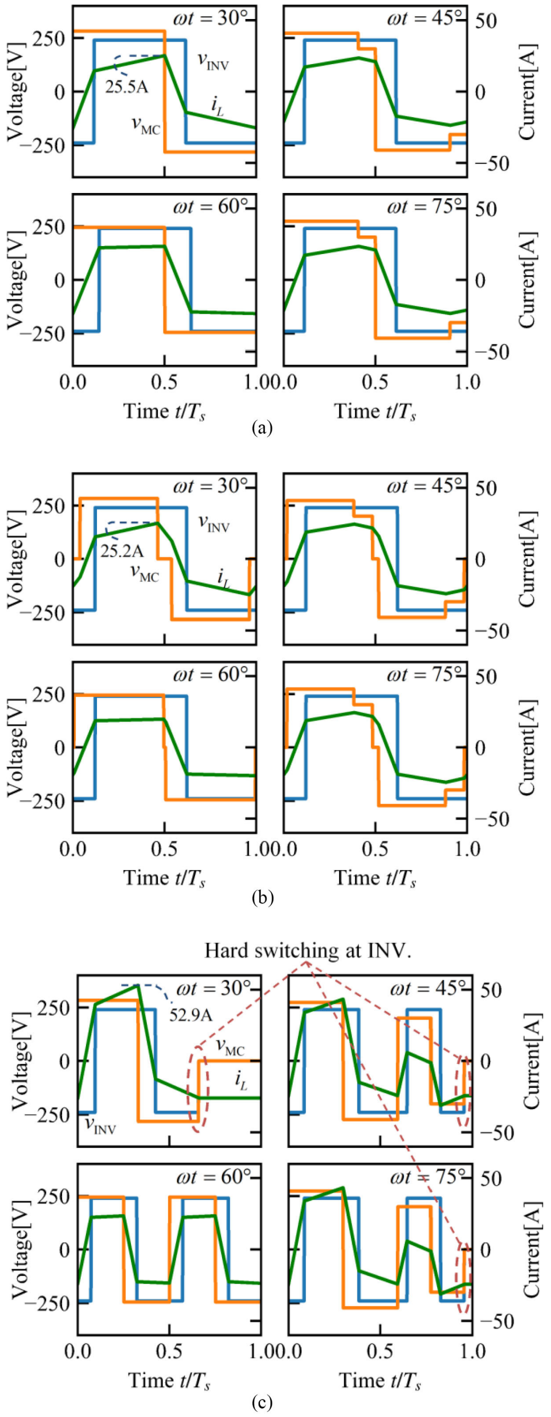

(a)

(b)

(c)

Fig. 15. Comparison of operation waveforms with two different existing methods. The simulation condition: $E = 200$V, $V_{\mathrm{dc}} = 240$ V, n = 1, $f = 100$kHz, $P^* = 4$ kW, $\alpha^* = 0$, $L = 17.8$ µH, and $T_s = 1/f$ (proposed method and [17]) and $2/f$([21]).(a) With peoposed method. (b) With method in [17]. (c) With method in [21].

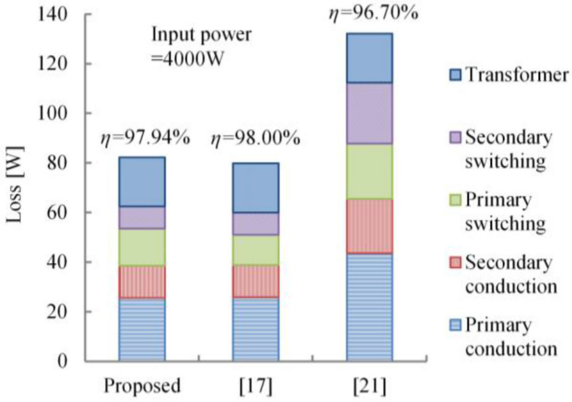

Fig. 16. Estimated losses and efficiency with each method. The conduction losses are calculated by ON-state resistance of a power switch R_{on} and the rms values of the currents of the high-frequency transformer that simulated by the equivalent circuit model (see Fig. 3). The switching losses are obtained by using a LUT that refers the current and the voltage waveforms of the high-frequency transformer. The efficiency of the transformer is assumed as 99.5% constant for simplify. The external inductor is treated as leakage inductance of integrated transformer. The power devices of MC and INV are supposed to SCT3017AL SiC MOSFET (ROHM). R_{on} is set to 17 mΩ. The LUT of the switching losses are created by using interpolation and extrapolation based on the provided characteristics of the switching losses. To simplify the calculation of the switching losses, the effect of the snubber capacitors is ignored.

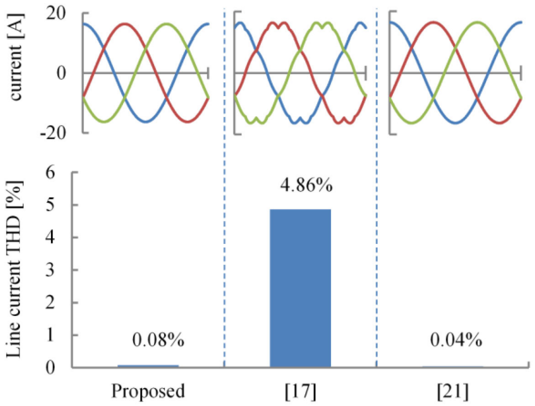

Fig. 17. Simulation results of the line current THD and waveforms with each method. Note that this is simulated by the equivalent circuit model (see Fig. 3) that does not include dynamics of the *LC* filter, switching time and losses of the each parts.

with the method in [21] is lower than others. The conduction losses and the secondary switching losses are especially larger than others. As previously mentioned, the conduction losses increases because of the large rms value of the i_L, and the switching losses increases because of the hard-switching in the INV. Fig. 17 shows the simulation results of the line current THD and waveforms with each method. The THD with the method in [17] is significantly larger than that of the others because of the lower accuracy of the control parameters obtained by using the trapezoidal approximation. The line current THD of lower than 0.1% is realized by the proposed method and the method in [21] because of higher accuracy of the control parameters. The THD of the proposed method is slightly larger than the method of [21]. This may be caused by the error of the numerical calculation.

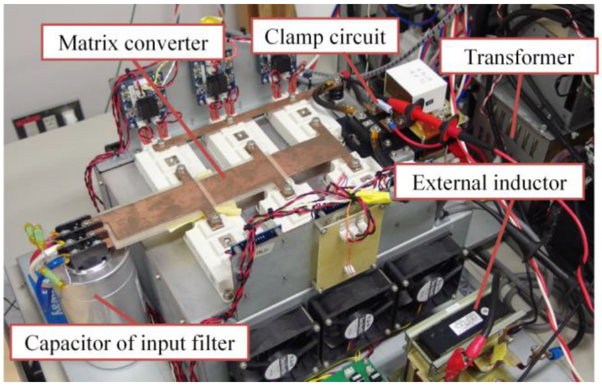

Fig. 18. Picture of the developed prototype system.

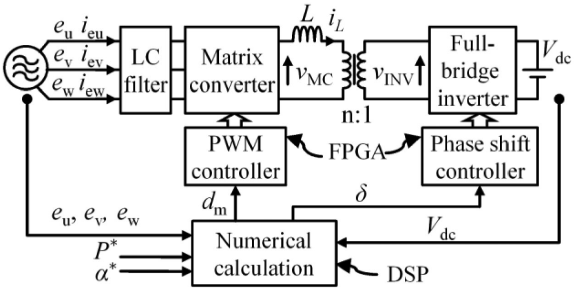

Fig. 19. Experimental system configuration.

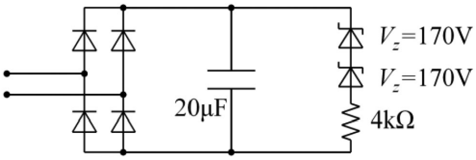

Fig. 20. Configuration of the clamp circuit.

From these results, it is confirmed that the proposed method can realize higher-efficiency as well as lower THD. This cannot be attained with the conventional methods proposed so far.

V. EXPERIMENTAL RESULTS

A. *System Configuration*

A 1-kW laboratory prototype shown in Fig. 18 was developed to confirm the validity of the proposed modulation method. Fig. 19 shows the system configuration and Table II gives the specifications of the system. The MC and INV are implemented with insulated gate bipolar transistor (IGBTs) and MOSFETs, respectively. The snubber capacitors are not installed. Note that the specifications of the prototype are not the same as those in the simulation in Section IV because the prototype was developed for the purpose of the verification of the basic functionality and the improvement of the waveforms with the proposed modulation method. A clamp circuit that protects the MC from the surge voltage caused by commutation failures is connected to the MC output terminals. The configuration of the

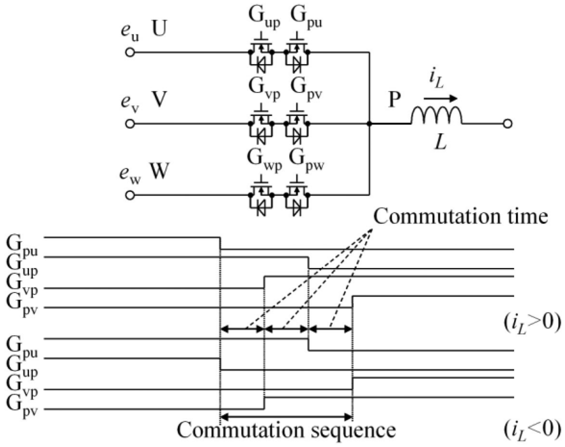

Fig. 21. Commutation sequence of the MC (commutation from *U* to *V*).

clamp circuit is shown in Fig. 20. The clamp circuit is implemented by using zener diodes. When the commutation failures do not occur, the voltage of the clamp circuit is kept constant 340 V by the characteristics of the zener diodes. Because this voltage is higher than the maximum value of the line voltages, the clamp circuit conducts only in the case of commutation failures without increasing steady-state losses. In the prototype, the ordinal four-step commutation sequence [28] is adopted. Fig. 21 shows an outline of the commutation sequence of the MC from *U* phase to *V* phase. The switching pattern depends on the sign of i_L. In the prototype, the sign of i_L is estimated based on the equivalent circuit of the high-frequency link (see Fig. 3). The controller is implemented with a digital signal processor (DSP) (TI: TMS320F28335) and an field programmable gate array (FPGA). The DSP calculates the duty ratio d_{m} and phase shift δ to realize sinusoidal line current the proposed method. The calculation is performed with bisection method, and the number of iterations in the numerical calculation is set to 10 to reduce the error of the control parameters small enough based on the result shown in Fig. 9. The total calculation time is less than 8.5 µs which is shorter than the one switching period. In the prototype system, the input power *P* and the power factor angle α are controlled in open-loop manner for given reference values P^* and α^*. Here, in the case of ac to dc conversion, *P* and P^* correspond to the ac input power. On the other hand, in the case of dc to ac conversion, they correspond to the dc input power.

B. Bidirectional Active Power Flow Control

This section presents the experimental results of bidirectional active power flow control. Fig. 22 shows the experimental waveforms in ac to dc conversion when the input power reference value $P^* = 1$kW and the power factor angle reference value $\alpha^* = 0°$. The line currents i_{eu}, i_{ev}, i_{ew} can be confirmed as sinusoidal waveforms. THD of the line currents is 3.9%. The phase difference between the phase voltages e_{u}, e_{v}, e_{w}, and the line currents is caused by leading reactive currents caused by the input *LC* filter. This phase difference can be reduced by adjusting parameters of the *LC* filter. The output voltages v_{MC} and v_{INV} of the MC and INV and the current of the high-frequency transformer i_L are high-frequency waveforms that mainly contain the switching frequency components. Fig. 23 shows the harmonic contents of the line current. It mainly contains low order harmonics. The largest harmonic component is fifth order (2.18% of the fundamental component) and all

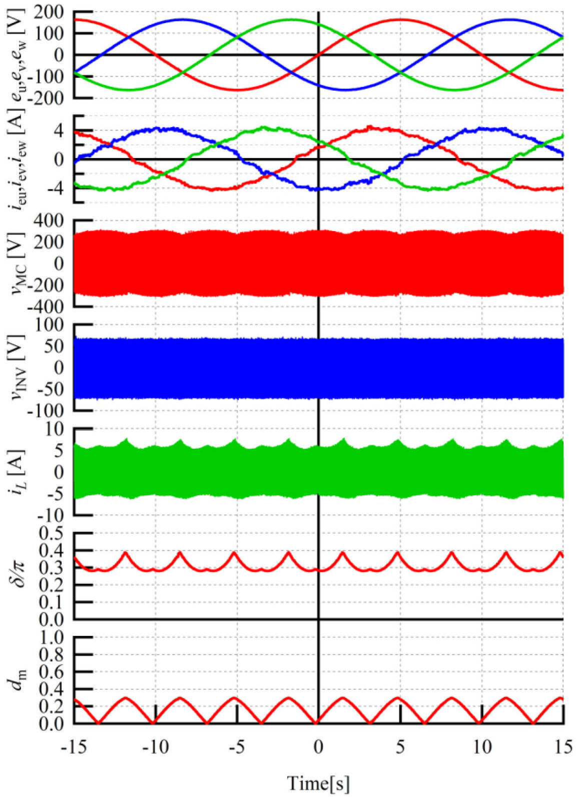

Fig. 22. Experimental waveforms in ac to dc conversion when $P^* = 1$kW and $\alpha^* = 0°$.

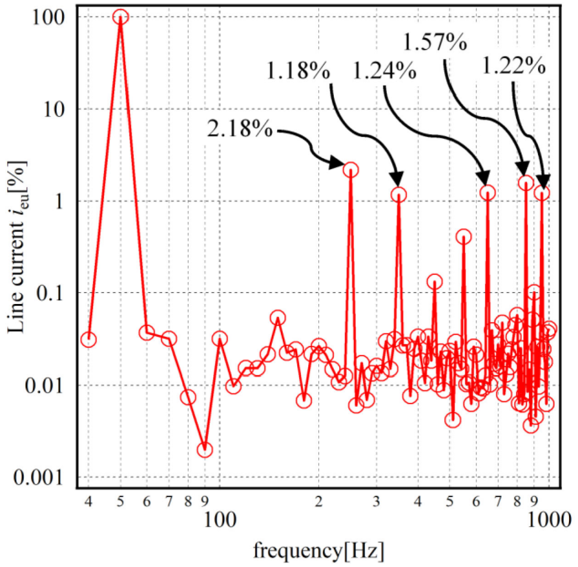

Fig. 23. Harmonic analysis of line current in ac to dc conversion when $P^* = 1$ kW and $\alpha^* = 0°$.

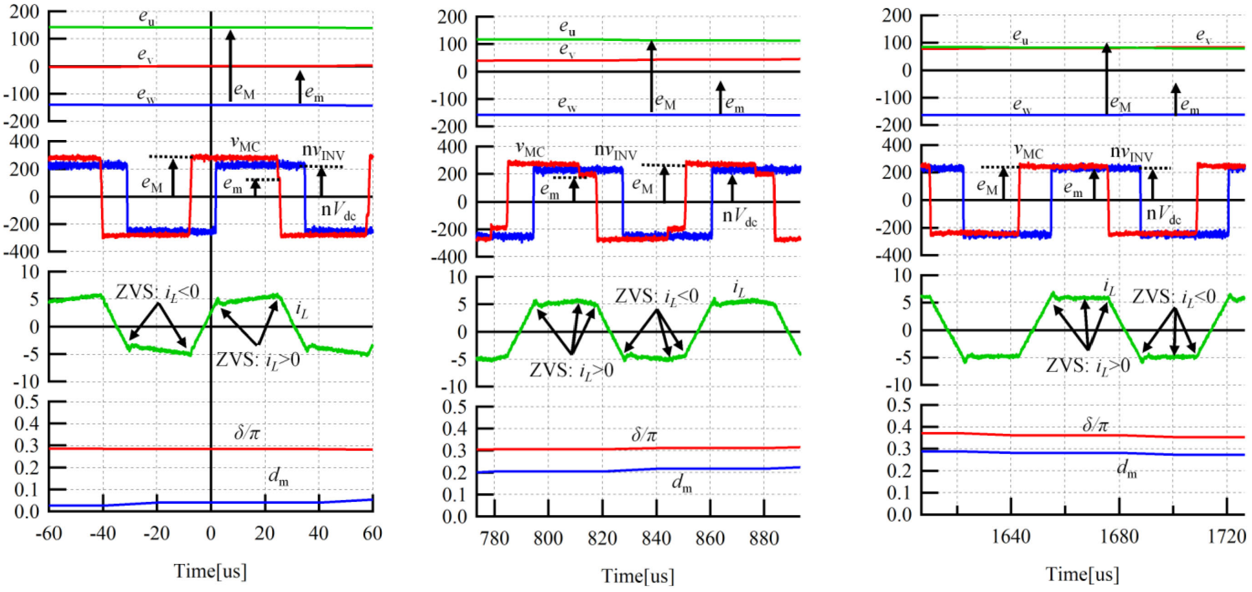

(a) (b) (c)

Fig. 24. Magnified waveforms for different phase angle of line voltage in ac to dc conversion when $P^* = 1$ kW. (a) $\theta = 30°$, $e_u > e_v = 0$ V, $i^*_{eu} > i^*_{ev} = 0$ A, $d_m \approx 0$. (b) $\theta = 45°$, $e_u > e_v > 0$ V, $i^*_{eu} > i^*_{ev} > 0$ A, $d_m > 0$. (c) $\theta = 60°$, $e_u = e_v > 0$ V, $i^*_{eu} = i^*_{ev} > 0$ A, $d_m > 0$.

harmonic components are less than 3%. They may be caused by the distortion of the input voltage source and periodical change in the control modes depending on the phase of the input voltages.

Fig. 24 shows the magnified voltage and current waveforms of the high-frequency transformer. It can be confirmed that the waveforms satisfy the ZVS condition at all switching cases. Fig. 24(a) shows the waveforms when the input voltage phase angle $\theta = \omega t$ is 30°. In this case, the input V phase voltage e_v is 0V, and the duty ratio d_m is about 0, and the waveform of v_{MC} is square wave which only consists of e_M. Fig. 24(b) shows the waveforms when θ is 45°. In this case, the input phase voltages satisfy $e_u > e_v > 0$, the duty ratio d_m is about 0.2, and the waveform of v_{MC} contains e_M and e_m. Fig. 24(c) shows the waveforms when θ is 60°. In this case, U phase voltage e_u equals to e_v, and the duty ratio d_m takes the maximum value (≈0.3).

Fig. 25 shows the experimental waveforms in dc to ac conversion when the input power reference value $P^* = 1$kW and the power factor angle reference value $\alpha^* = 0°$. The sinusoidal waveforms of the line currents are also observed in this case and THD of the line current is 3.7%.

From these results, it is confirmed that the proposed method can realize the sinusoidal line currents with THD of less than 4% under the bidirectional operating conditions at the rated power.

Fig. 26 shows measured THD characteristics of the line current by using HIOKI PW6001 power analyzer. The THD of the line currents is less than 5% under heavy load conditions in bidirectional operation. In the case of ac to dc conversion, THD is less than 5% in the operation range above 500 W. The characteristics of ac to dc conversion and dc to ac conversion are not the same, and the line current THD in dc to ac conversion is significantly larger than that in ac to dc conversion when the transmitted power is less than 700 W. Fig. 27 shows relationship between the input power P and the reference value P^*. Similar to the characteristics of THD, the characteristics of P in ac to dc conversion and dc to ac conversion are different. The difference between P and P^* in dc to ac conversion becomes significant when the power is less than 700 W. These results are caused by

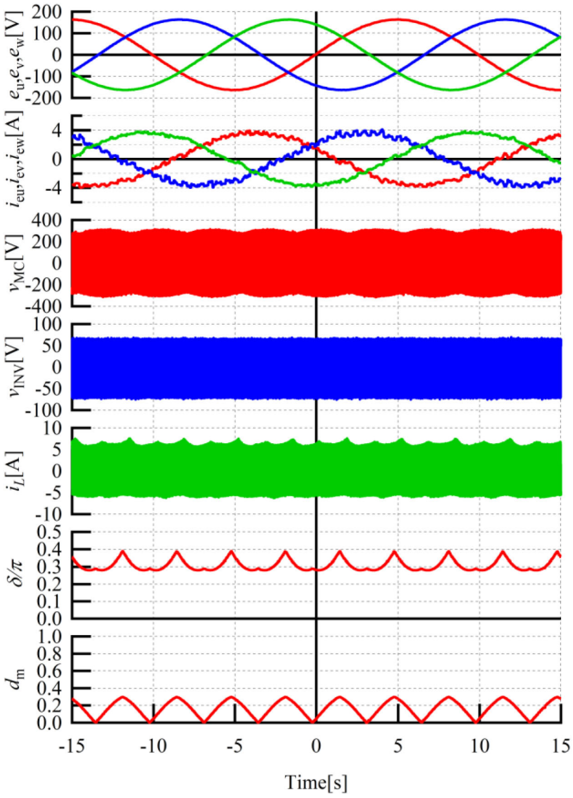

Fig. 25. Experimental waveforms in dc to ac conversion when $P^* = 1$ kW and $\alpha^* = 0°$.

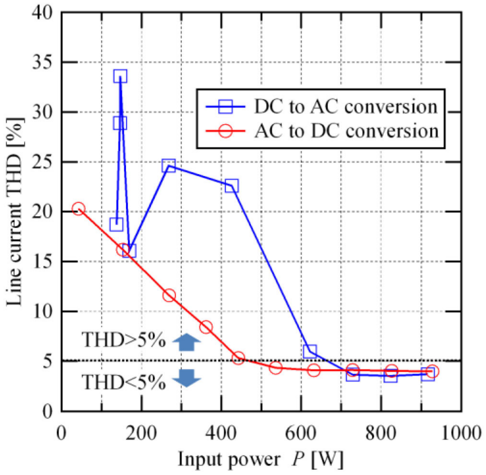

Fig. 26. Measured characteristics of line current THD.

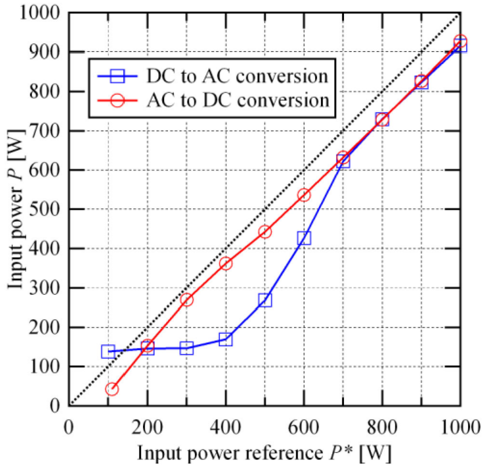

Fig. 27. Relationship between input power P and its reference P^*.

the difference in the dead time of the INV and the commutation time of the MC. Fig. 28 shows the effect of the dead time and the commutation time. In dc to ac conversion, the rate of change in i_L increases after the switching of the INV. In the same way, in ac to dc conversion, i_L increases after the switching of the MC. If the sign of i_L changes during the dead time or the commutation time, the voltage error and hard switching occur. Thus, the voltage error tends to occur under longer dead time or commutation time. This error causes reduction in the power and increase in the THD of the line currents. In dc to ac conversion, this effect occurs around $P^*<700$ W. In contrast, this effect does not occur in ac to dc conversion. The difference in the effect may be caused by the difference of the dead time and the commutation time. In the laboratory prototype, the dead time of the INV is set to 3μs, and the commutation time of one step sequence of the MC is set to 1.5μs. If the dead time is short enough, the line current THD and the difference of between P and P^* can be reduced in wider operation range.

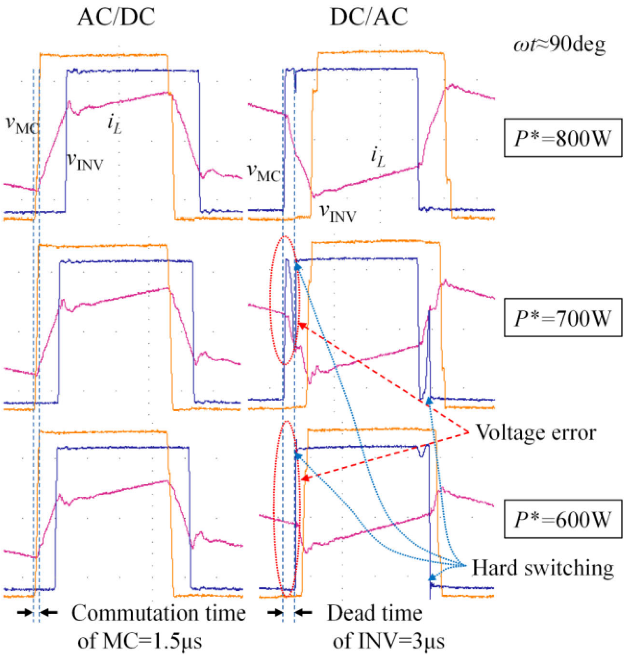

Fig. 28. Effect of dead time and commutation time.

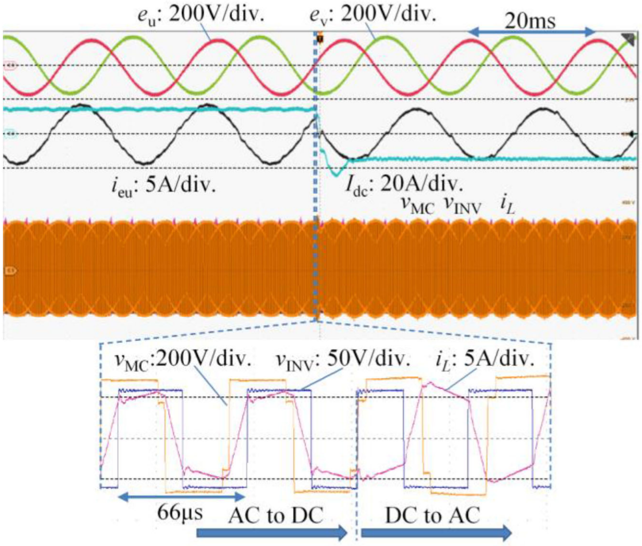

Fig. 29. Waveforms at a sudden change in power direction. ($P^* = 1$ kW and $\alpha^* = 0°$).

Fig. 29 shows the waveforms at a sudden change in the direction of power flow. The direction of power is switched from ac to dc conversion to dc to ac conversion at the instant of the center of figure. The input line current i_{eu} changes immediately, and stabilized to sinusoidal waveform. The bottom of the figure shows the magnified voltage and current waveforms of the high-frequency transformer. Improper waveforms do not occur, and it can be confirmed that the change in the power direction is realized seamlessly.

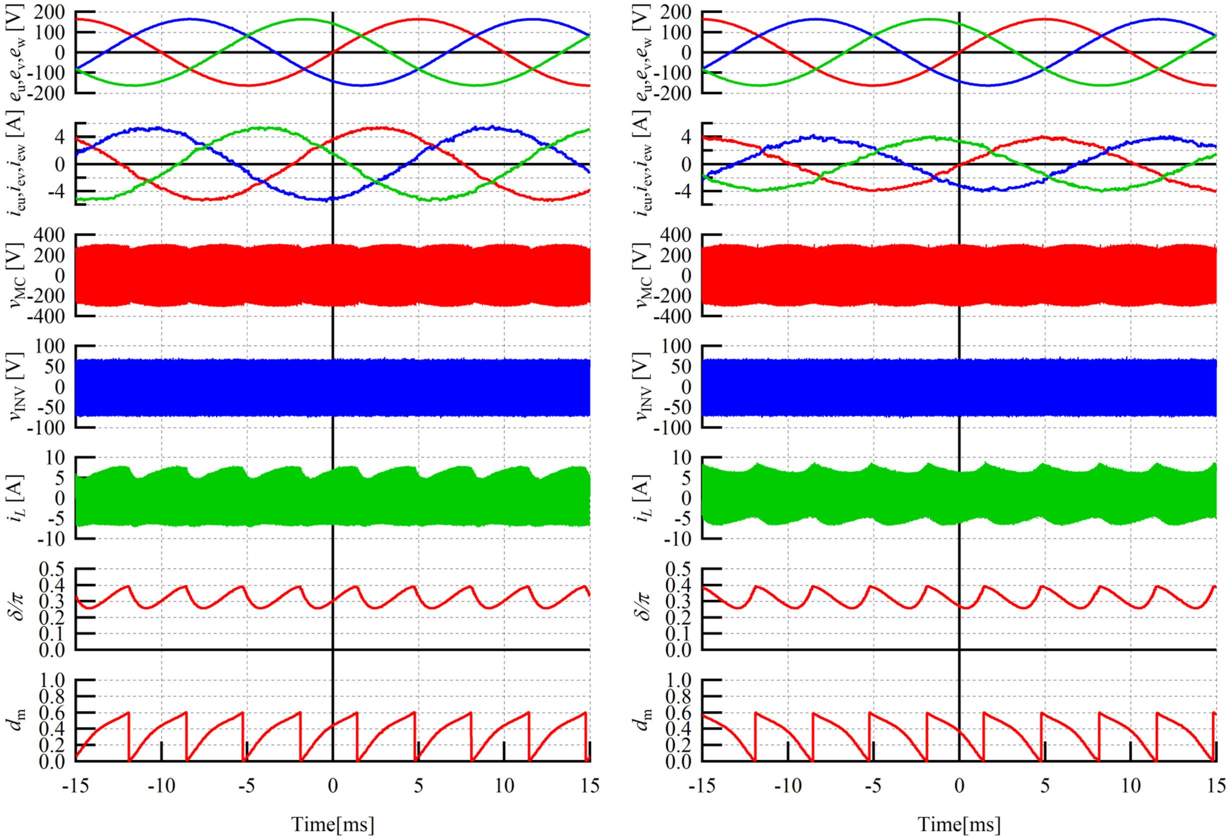

(a) (b)

Fig. 30. Experimental waveforms under reactive power flow control (ac to dc conversion, $P^* = 1$ kW). (a) $\alpha^* = -30°$. (b) $\alpha^* = +30°$.

TABLE III

EXPERIMENTAL CHARACTERISTICS OF REACTIVE POWER (α^*: POWER FACTOR ANGLE REFERENCE VALUE, P: AVERAGE INPUT ACTIVE POWER, Q: AVERAGE INPUT REACTIVE POWER, AND α: POWER FACTOR ANGLE) ($P^* = 1$ kW)

(a) Reactive power containing leading current of LC filter.

α*[°]	*P*[W]	*Q*[var]	α[°]
-30	923	-956	-46.0
0	927	-474	-27.1
30	922	-9.98	-0.621

(b) Reactive power neglecting leading current of LC filter.

α*[°]	*P*[W]	*Q*[var]	α[°]
-30	923	-482	-27.6
0	927	-0	0
30	922	-464	26.7

C. Reactive Power Flow Control

This section presents experimental results of reactive power control. In the case when $\alpha^* = -30°$, as shown in Fig. 30(a) the phase of the line current $i_{\mathrm{eu}}, i_{\mathrm{ev}}, i_{\mathrm{ew}}$ leads compared with the case of $\alpha^* = 0°$ (see Fig. 22). In the same way, the phase of line current in the case of $\alpha^* = 30°$ [see Fig. 30(b)] lags compared with the case of $\alpha^* = 0°$ (see Fig. 22). In addition, the waveforms of line currents are sinusoidal in both cases. The THD of line current when $\alpha^* = -30°$ and $\alpha^* = 30°$ are 1.9% and 3.8%, respectively.

The characteristics of the average reactive power Q and the power factor angle α are shown in Table III(a). The power factor angle α does not coincide with its reference α^* because the leading current of the input *LC* filter is included in the line current. Table III(b) gives the result when the leading currents of the *LC* filter are neglected. In this case, the power factor angle almost coincides with its reference. From these results, it is confirmed that the proposed method can control bidirectional reactive power flow. Therefore, the proposed method can compensate the leading current of the *LC* filter by adjusting the power factor reference value α^* and can realize unity power factor. In fact, it can be confirmed that the leading current of the *LC* filter is almost canceled by adjusting the power factor angle of the converter in Fig. 30(b).

D. Efficiency and Loss Distribution

Fig. 31 shows the system efficiency in bidirectional operations. The maximum efficiency is 90.3% in ac to dc conversion. In dc to ac conversion, the efficiency decreases when P<600 W because the voltage error and the hard switching occur as described in Section V-B. In addition, the efficiency in dc to ac conversion is lower overall than ac to dc conversion. This can be considered as a result of the voltage drop of the power devices. In general, the efficiency of DAB converters decreases with larger

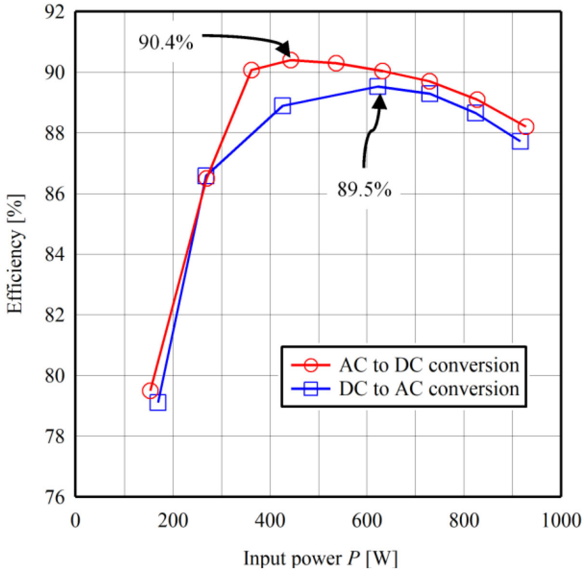

Fig. 31. System efficiency.

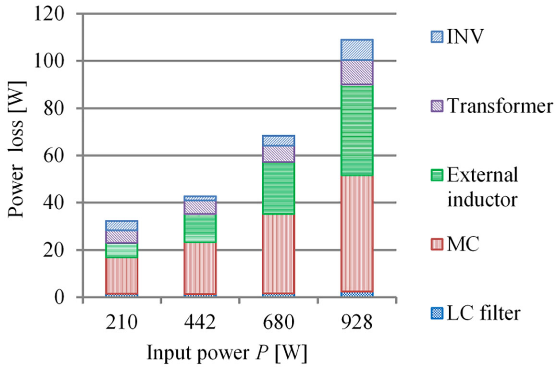

Fig. 32. Measured loss distribution in ac to dc conversion.

difference between the input voltage and output voltage referred to the primary side of the transformer because the reactive current of the transformer increases. In the prototype, the input voltage is higher than the output voltage referred to the primary side. Therefore, in ac to dc conversion, the voltage difference is reduced by the voltage drop of the power devices. On the other hand, the difference in the voltages increased in dc to ac conversion, resulting in the lower efficiency than ac to dc conversion. The measured rms value of i_L when $P^* = 1$ kW in dc to ac conversion and ac to dc conversion are 3.87 and 3.75 A, respectively.

Fig. 32 shows measured loss distribution in ac to dc conversion. The power at each stage of the converter was measured directly by using HIOKI PW6001 power analyzer with clamp type current probes. The losses in the MC and external inductor are dominant, and they take 80% of the total loss when $P = 928$ W. The large loss is caused due to large high frequency resistance of a flat wire used in the external inductor. An external inductor implemented by litz wire or integrated high-frequency transformer with required leakage inductance would improve the system efficiency. In addition, application of high-performance power device, such as SiC-MOSFET or GaN-high electron mobility transistor (HEMT) to MC can reduce loss significantly. In fact, the estimated efficiency shown in Fig. 16 is almost 98% at 4 kW with SiC MOSFETs and a high efficiency transformer. Moreover, addition of the snubber capacitor can also reduce the switching losses.

VI. CONCLUSION

This article presented an improved modulation method of the bidirectional isolated ac/dc DAB converters based on matrix converter. The proposed method can achieve sinusoidal line currents and ZVS under bidirectional operation. To realize sinusoidal line currents, the accurate duty cycle d_{m} and the phase shift δ are determined by using real time numerical calculation based on the nonlinear system mathematical model.

The simulation work, in this article, has demonstrated the dynamic performance with *PQ* control. The simulation results based on the equivalent circuit model have shown that the proposed method can realize both low input current THD and higher-efficiency compared with the existing *PQ* controllable methods. The simulation results also confirmed that the system efficiency can achieve around 98% at 100 kHz, 4 kW with SiC-MOSFETs. In this simulation, the effect of the snubber capacitor is neglected to simplify the calculation. The appropriate snubber capacitor might improve the maximum system efficiency at heavy load conditions.

To confirm the effectiveness of the proposed modulation, experimental work employing a 1-kW laboratory prototype has been performed. It has been demonstrated that sinusoidal line current with THD of less than 5% under bidirectional operations can be realized. The ZVS conditions were confirmed at all switching by the current and voltage waveforms in high-frequency transformer.

REFERENCES

[1] M. T. Lawder *et al.*, “Battery Energy storage system (BESS) and battery management system (BMS) for grid-scale applications,” *Proc. IEEE*, vol. 102, no. 6, pp. 1014–1030, May 2014.

[2] B. Singh, B. N. Singh, A. Chandra, K. Al-Haddad, A. Pandey, and D. P. Kothari, “A review of three-phase improved power quality AC-DC converters,” *IEEE Trans. Ind. Electronics*, vol. 51, no. 3, pp. 641–660, Jun. 2004.

[3] M. Jain, M. Daniele, and P. K. Jain, “A bidirectional DC-DC converter topology for low power application,” *IEEE Trans. Power Electron.*, vol. 15, no. 4, pp. 595–606, Jul. 2000.

[4] S. Inoue and H. Akagi, “A bidirectional DC–DC Converter for an energy storage system with galvanic isolation,” *IEEE Trans. Power Electron.*, vol. 22, no. 6, pp. 2299–2306, Nov. 2007.

[5] M. Yilmaz and P. T. Krein, “Review of battery charger topologies, charging power levels, and infrastructure for plug-in electric and hybrid vehicles,” *IEEE Trans. Power Electron.*, vol. 28, no. 5, pp. 2151–2169, May 2013.

[6] S. Manias and P. D. Ziogas, ”A novel sine wave in AC to DC converter with high-frequency transformer isolation,” *IEEE Trans. Ind. Electron.*, vol. 32, no. 4, pp. 430–438, Nov. 1985.

[7] D. De and V. Ramanarayanan, ”A DC-to-Three-Phase-AC High-frequency link converter with compensation for nonlinear distortion,” *IEEE Trans. Ind. Electron.*, vol. 57, no. 11, pp. 3669–3677, Nov. 2010.

[8] M. Yamada, and T. Takeshita, "PWM strategy of AC to DC Converter with high frequency link for reducing output voltage ripple," in *Proc. 4th Int. Conf. Power Eng., Energy Elect. Drives*, 2013, pp. 846–851.

[9] K. Inagaki and S. Okum, "A high frequency Link DC/AC converter using a three-phase output PWM controlled cycloconverter," *IEEJ Trans. Ind. Appl.*, vol. 112, no. 6, pp. 545–552, Jun. 1992.

[10] S. Norrga, S. Meier, and S. "Ostlund, "A three-phase soft-switched isolated AC/DC converter without auxiliary circuit," *IEEE Trans. Ind. Electron.*, vol. 44, no. 3, pp. 836–844, May 2008.

[11] S. Takuma, K. Orikawa, J. Itoh, R. Oshima, and H Takahashi, "Isolated DC to three-phase AC converter using indirect matrix converter with ZVS applied to all switches," in *Proc. IEEE Energy Convers. Congr. Expo.*, Oct. 2015, pp. 4678–4689.

[12] J. Everts, F. Krismer, J. V. D. Keybus, J. Driesen, and J. W. Kolar, "Optimal ZVS modulation of single-phase single-stage bidirectional DAB AC–DC Converters," *IEEE Trans. Power Electron.*, vol. 29, no. 8, pp. 3954–3970, Aug. 2014.

[13] N. Weise, K. Basu, and N. Mohan, "Advanced modulation strategy for a three-phase ac-dc dual active bridge for v2g," in *Proc. IEEE Veh. Power Propulsion Conf.*, 2011, pp. 1–6.

[14] D. Das, N. Weise, R. Baranwal, and N. Mohan, "A bidirectional soft-switched DAB-based single-stage three-phase AC–DC converter for V2G application," *IEEE Trans. Trans. Electron.*, vol. 5, no. 1, pp. 186–199, Mar. 2019.

[15] M. A. Sayed, K. Suzuki, T. Takeshita, and W. Kitagawa, "PWM switching technique for three-phase bidirectional grid-tie DC-AC-AC converter with high-frequency isolation," *IEEE Trans. Power Electron.*, vol. 33, no. 1, pp. 845–858, Jan. 2018.

[16] M. A. Sayed, K. Suzuki, T. Takeshita, and W. Kitagawa, "Soft-switching PWM technique for grid-tie isolated bidirectional DC-AC converter with SiC device," *IEEE Trans. Ind. Appl.*, vol. 53, no. 6, pp. 5602–5614, Jul. 2017.

[17] M. A. Sayed, T. Takeshita, and W. Kitagawa, "Advanced PWM switching technique for accurate unity power factor of bidirectional three-phase grid-tied DC-AC converters," *IEEE Trans. Ind. Appl.*, vol. 55, no. 6, pp. 7614–7627, Dec. 2019.

[18] S. Takuma, K. Kusaka, J. Itoh, Y. Ohnuma, and S. Miyawaki, "A novel current ripple cancellation PWM for isolated three-phase matrix DAB AC-DC matrix converter," in *Proc. 21st Eur. Conf. Power Electron. Appl.*, Sep. 2019, pp. 1–10.

[19] W. Wu and X. Li, "Improved modulation for dual active bridge based three-phase single-stage AC-DC converter," *IEEE Convers. Congr. Expo.*, Sep. 2019, pp. 2135–2140.

[20] P. Nayak and K. Rajashekara, "An asymmetrical space vector PWM scheme for a three phase single-stage DC-AC Converter," in *Proc. IEEE Convers. Congr. Expo.*, Sep. 2019, pp. 635–639.

[21] D. Varajão, R. E. Araùjo, L. M. Miranda, and J. A. P. Lopes, "Modulation Strategy for a Single-Stage Bidirectional and Isolated AC-DC matrix converter for energy storage systems," *IEEE Trans. Ind. Electron,*, vol. 65, no. 4, pp. 3458–3468, Sep. 2018.

[22] W. Deng, H. Liu, and Y. Liu, "A new control method for bidirectional isolated AC/DC matrix converter," in *Proc. 22nd Int. Conf. Elect, Mach. Syst.*, Aug. 2019, pp. 1–6.

[23] L. Schrittwieser, M. Leibl, and J. W. Kolar "99% efficient isolated three-phase matrix-type DAB buck-boost PFC rectifier," *IEEE Trans. Power Electron.*, vol. 35, no. 1, pp. 138–157, Jan. 2020.

[24] R.W. De Doncker, D.M. Divan, and M. H. Kheraluwala, "A three-phase soft-switched high-power-density DC/DC converter for high-power applications," *IEEE Trans. Ind. Appl.*, vol. 27, no. 1, pp. 63–73, Jan. 1991.

[25] B. Zhao, Q. Song, W. Liu, and Y. Sun, "Overview of Dual-Active-Bridge Isolated Bidirectional DC–DC converter for high-frequency-link power-conversion system," *IEEE Trans. Power Electron.*, vol. 29, no. 8, pp. 4091–4106, Aug. 2014.

[26] K. Shigeuchi, J. Xu, N. Shimosato, and Y. Sato, "A new modulation method applying optimal duty cycle and phase shift for bidirectional isolated three-phase AC/DC converter based on matrix converter," in *Proc. Int. Power Electron. Conf.*, 2018, pp. 3514–3521.

[27] A. K. Singh, P. P. Deshpande, and S. K. Panda, "The input displacement power factor compensation of a matrix based isolated bidirectional AC-DC converter," in *Proc. Innov. Smart Grid Technol.-Asia*, May 2018, pp. 260–264,.

[28] P. W. Wheeler, J. Rodríguez, J. C. Clare, L. Empringham, and A. Weinstein, "Matrix Converters: A technology review," *IEEE Trans. Ind. Electron.*, vol. 49, no. 2, pp. 276–288, Aug. 2002.

Koji Shigeuchi received the B.E. and M.E. degrees in electrical engineering from Chiba University, Chiba, Japan, in 2016, and 2018, respectively.

Since 2018, he has been with Toyota Central R&D Labs, Inc., Nagakute, Japan. His research interests include design, control and application of power electronics, such as isolated dc/dc converter, isolated ac/dc converter using matrix converter.

Mr. Shigeuchi is a member of the Institute of Electrical Engineers of Japan. He was the recipient of the Paper Presentation Award 2018 from IEEJ and the IPEC-Niigata 2018—ECCE Asia Third Prize Paper Award.

Jin Xu (Member, IEEE) received the B.E. degree from the Harbin University of Science and Technology, Harbin, China, in 2004, and the M.E. and D.E. degrees from Chiba University, Chiba, Japan, in 2009, 2012, respectively.

From 2009 to 2012, he was with the National Institute of Advanced Industrial Science and Technology, as a Technical Staff, Tsukuba, Japan. Since 2012, he has been with Myway Plus Corporation, Yokohama, Japan. His research interests include design, control and application of power electronics, such as isolated dc/dc converter, multiphase converter, multilevel inverter, high frequency isolated ac/dc converter using matrix converter, regenerative dc power supply, etc.

Mr. Xu is a member of the IEEJ.

Noboru Shimosato (Member, IEEE) received the B.E. and M.E. degrees from the Kanagawa Institute of Technology, Kanagawa, Japan, in 2005, 2007, respectively.

Since 2007, he has been with Myway Plus Corporation, Yokohama, Japan. His research interests include design, control and application of power electronics, such as regenerative dc power supply, regenerative ac electronic load, etc.

Mr. Shimosato is a member of the IEEJ.

Yukihiko Sato (Member, IEEE) received the B. Eng., M. Eng., and D. Eng. degrees from the Tokyo Institute of Technology, Tokyo, Japan, in 1986, 1988, and 1995, respectively.

From 1988 to 2001, he was with the Tokyo Institute of Technology, as a Research Associate and an Associate Professor. Since 2001, he has been with Chiba University, Chiba, Japan, where he is currently a Professor and the Dean of Graduate School of Engineering. His current research interests include control and circuit topologies of power converters.

Dr. Sato is a Senior Member of IEEJ.